Available online at www.sciencedirect.com
SCIENCE DIRECT®
Aerospace Science and Technology 7 (2003) 263–275
Aerospace Science and Technology
www.elsevier.com/locate/aescte

Analysis of wake vortex decay mechanisms in the atmosphere ☆

Analyse der Zerfallsmechanismen von Wirbelschleppen in der Atmosphäre

Frank Holzäpfel [a,*], Thomas Hofbauer [a], Denis Darracq [b], Henri Moet [b], François Garnier [c], Cecile Ferreira Gago [c]

[a] *Institut für Physik der Atmosphäre, DLR Oberpfaffenhofen, 82234 Weßling, Germany*
[b] *CERFACS, 31057 Toulouse, France*
[c] *Département de Physique Unité d'Environnement Atmosphérique, ONERA, 92320 Châtillon, France*

Received 10 October 2001; received in revised form 13 December 2002; accepted 26 February 2003

Abstract

Results of high-resolution numerical simulations of aircraft wake vortex evolution and decay in different regimes and atmospheric conditions are presented. The different cases comprise (i) the near field interaction of a trailing vortex with an exhaust jet, (ii) the evolution of single vortices and counter-rotating vortex pairs in homogeneous isotropic turbulence, as well as (iii) the decay of wake vortices in a turbulent stably stratified atmosphere, and (iv) in a weakly turbulent sheared environment. The different cases are used to analyse common aspects of vortex dynamics and decay mechanisms. In all scenarios the formation of coherent secondary vorticity structures that enclose the primary vortices is observed. These secondary vorticity structures deform and weaken the primary vortices and in some cases lead to rapid vortex decay. It is shown that the mean swirling flow effectively rearranges and intensifies any secondary vorticity by tilting and stretching. The secondary vorticity may either originate from the turbine jet, ambient turbulence or may be produced baroclinically. Based on the observed phenomena, eleven postulates are established that pinpoint fundamental aspects of the observed decay mechanisms.

Zusammenfassung

Mittels hochauflösender numerischer Simulationen wird die Entwicklung und der Zerfall von Flugzeug-Wirbelschleppen unter verschiedenen atmosphärischen Bedingungen untersucht. Die betrachteten Szenarien umfassen (i) die Wechselwirkung eines Triebwerksstrahls mit einem Nachlaufwirbel, (ii) die Entwicklung von Einzelwirbeln und gegensinnig rotierenden Wirbelpaaren in homogener isotroper Turbulenz, (iii) den Wirbelschleppenzerfall in einer turbulenten stabil geschichteten Atmosphäre und (iv) in einer schwach turbulenten Umgebung mit überlagerter Windscherung. Die Untersuchungen konzentrieren sich auf den verschiedenen Fällen gemeinsame Aspekte der Wirbeldynamik und des Zerfalls. Stets werden kohärente Sekundärwirbelstrukturen beobachtet, die die Primärwirbel umschließen. Die Sekundärwirbel deformieren und schwächen die Wirbelschleppe und können ihren schnellen Zerfall auslösen. Es wird gezeigt, dass die mittlere Wirbelströmung die zunächst inkohärente sekundäre Wirbelstärke in effektiver Weise durch Kippen umorganisiert und mittels Streckung verstärkt. Die sekundäre Wirbelstärke kann durch den Triebwerksstrahl, die Umgebungsturbulenz oder barokline Produktion eingebracht werden. Es werden elf Postulate aufgestellt, die wesentliche Aspekte der beobachteten Zerfallsmechanismen beschreiben.

Keywords: Wake vortices; Numerical simulation; Exhaust jet; Turbulence; Stable stratification; Shear; Secondary vorticity structures

Schlüsselwörter: Wirbelschleppe; Numerische Simulation; Triebwerksstrahl; Turbulenz; Stabile Schichtung; Scherung; Sekundärwirbelstrukturen

☆ This article was presented at ODAS 2001.

* Corresponding author.
E-mail address: frank.holzaepfel@dlr.de (F. Holzäpfel).

1270-9638/03/$ – see front matter
doi:10.1016/S1270-9638(03)00026-9

1. Introduction

The lift exerted on aircraft wings produces long-lived trailing vortices. Especially during an aircraft's critical landing phase these can endanger following aircraft. To avoid wake vortex encounters, follower aircraft must maintain a safe distance to a landing aircraft up ahead of them. In order to increase airport capacities whilst at least maintaining safety levels, the knowledge of wake vortex behaviour under varying meteorological conditions achieves considerable significance. Also, the influence of aircraft design on the strength of the shed vortices and the related potentially more rapid decay is of crucial importance.

The mostly prevailing decay mechanism in cruise altitude, the so-called Crow instability [2], can frequently be observed being visualized by contrails. Minor atmospheric turbulence is sufficient to trigger sinusoidal oscillations of the vortices that lead to vortex reconnection and, finally, the formation of descending vortex rings. Although the Crow instability is well understood in principle, the longevity of vortex rings and their effects on encountering aircraft are discussed controversly.

Another controversy applies to the temporal evolution of vortex intensity and decay. Two radically different concepts are debated, namely the concept of gradual and predictable decay and the concept of stochastic collapse [30]. In the latter concept a phase of minor gradual decay is followed by a rapid decay phase [9] which coincides with a transition to fully turbulent vortices [15,26]. The controversy can in part be resolved by the insight that the observed circulation evolution largely depends on its definition. On small radii a gradual decay is observed which reflects diffusion in the vortex core region, whereas larger radii are not affected by this diffusion and rapid circulation decay sets only in when instability mechanisms have developed. On the other hand, rapid decay could well be masked in lidar[1] measurements due to several reasons: (i) gradual spatial deformation of vortices will apparently decrease gradually swirl velocities in the measurement plane, (ii) the advection of deformed vortices through the measurement plane will cause substantial scatter. If that scatter shall be reduced by averaging of circulation data from several flights, characteristic features of circulation evolution are smeared out, (iii) the late phase of potentially rapid circulation decay is not accessible by lidar probably because vortices decay turbulently [15] or can not be distinguished from their turbulent environment. So numerical approaches have to be employed to contribute to a comprehensive understanding of vortex decay characteristics. The above mentioned and further implications of circulation evaluation from lidar data are discussed in detail in [16].

In-situ measurements in the wakes of various aircraft have shown that the exhaust jets contribute dominantly to aircraft-induced wake turbulence compared to other sources like boundary layer separation [14]. So the turbine jet constitutes a top candidate to affect wake evolution by aircraft design. Turbulence, stratification and shear, on the other hand, are the primary influences on vortex evolution in the atmosphere. All the mentioned scenarios are tackled in this manuscript. Merely, the effect of ground proximity is not considered.

In the current article, a condensed survey is given on four wake vortex calculations that were in part already described in previous publications. In each of the four cases different numerical approaches and parameters are applied (cf. Table 1). A detailed description of the approaches would go beyond the scope of this paper and is given elsewhere [6,11,14,24]. However, the dissimilar pecularities of the described approaches on one hand, and the similar topologies of the resulting vortex evolutions on the other hand, indicate a relative independency of results from specific methodological aspects. This finding encourages us to consider the extracted common aspects of wake vortex decay as generic and universally valid results. The analysed phenomena are related to the formation of coherent secondary vorticity structures and their impact on vortex decay. We argue that the observed effects, though extremely difficult to verify experimentally, generally occur in wake vortex evolution and play a crucial role for vortex decay. Based on the current results, eleven postulates are derived that characterize prominent mechanisms of wake vortex decay. The interrelation of azimuthal vorticity structures and wake vortex decay was first pointed out by Risso et al. [27] and is typical for three-dimensional turbulence initialization [19].

2. Vortex jet interaction

In the near field of the aircraft wake the exhaust jets of the turbines are entrained into the two counter-rotating wingtip vortices which at the same time roll up from the sheet of vorticity induced by the wings [7]. To investigate the highly complex entrainment and mixing process of the turbulent jet into a trailing vortex it is convenient to identify two overlapping regimes [5,22]: the jet regime and the deflection regime. In the current numerical approach these two regimes are modeled sequentially. First the turbulent jet evolves temporarily and uninfluenced by the wake flow. Then in the deflection regime the interaction of jet and wake flow is modeled. The characteristic dimensions of the numerical set-up are provided by a wind tunnel experiment [1] and are based on similarity parameters of a large transport aircraft with two engine jets. The experimental results show that the vortex flow does not affect the engine jet behaviour until a downstream distance of 0.5–1 wing spans. For modern large transport aircraft, the characteristic size of the jet regime is of the order of 1–50 diameters of the nozzle exit, while the deflection regime, scaled to the wingspan, extends

[1] LIght Detection And Ranging, remote sensing technique to measure the line-of-sight velocity along a Laser beam that scans wake vortices.

Table 1
Survey of cases, numerical codes, methods, vortex Reynolds numbers, $Re = \Gamma/\nu$, boundary conditions in flight direction, x, lateral direction, y, and vertical direction, z (per. stands for periodic and nr. for non-reflecting), ratio of domain size, L, to vortex core radius, r_c, and number of grid points across core radius

Case	Jet (Section 2)	HIT (Section 3)	Strat (Section 4)	Shear (Section 5)
Code	PEGASE [6]	NTMIX3D [31]	LESTUF [18]	MESOSCOP [28]
Method	DNS	LES	LES	DNS
Re	5000 (jet: 1000)	$100 \cdot 10^6$	∞	2200
Boundary conditions	per. × nr. × nr.	periodic	periodic	per. × per. × free slip
$L_x/r_c \times L_y/r_c \times L_z/r_c$	$12 \times 66.9 \times 66.9$	28.2^3; 28.2×56.4^2(SV$_{5.5}$)	$102 \times 64 \times 135$	$68.8 \times 128 \times 85.3$
$r_c/\Delta x \times r_c/\Delta y \times r_c/\Delta z$	$7.5 \times 10 \times 10$	2.3^3	$0.63 \times 4 \times 4$	$0.93 \times 3 \times 3$

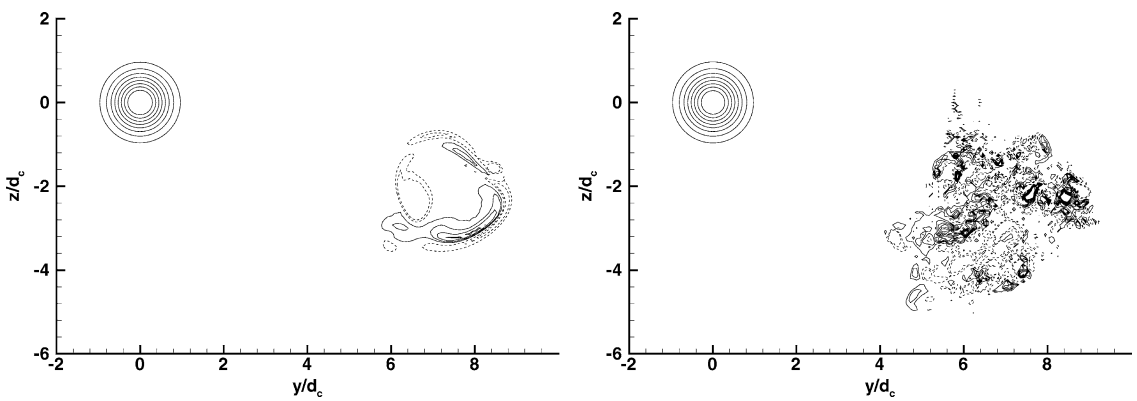

Fig. 1. Normalized axial vorticity contours in a vertical lateral cross-section at $x/B = 0.5$ (left) and $x/B = 1$ (right). Dashed lines denote negative vorticity; contour range from -1 to 4 in steps of 0.5.

downstream of the airplane to a distance of about 1–10 wingspans.

The simulations are performed with a temporal DNS of the three-dimensional Navier–Stokes equations. Key parameters of all simulations are listed in Table 1. For details of the numerical method we refer to [6]. The axial length of the domain of 6 nozzle radii corresponds to twice the wavelength of the maximum growth rate of the first azimuthal instability of a spatially evolving jet [23]. An unstable nozzle outlet velocity profile [23] is prescribed which is superimposed by three-dimensional Gaussian shape random perturbations. When the jet simulation has reached an age that corresponds to a downstream distance of 0.5 wing spans ($x/B = 0.5$), the cross-section of the domain is enlarged and a Lamb–Oseen vortex is superimposed on the flow field at a distance of 14 vortex core radii from the jet center (Fig. 1).

The tangential velocity profile, $v_\theta(r)$, of the Lamb–Oseen vortex is given by

$$v_\theta(r) = \frac{1.4 v_0 r_c}{r}\left(1 - \exp\frac{-1.256 r^2}{r_c^2}\right), \tag{1}$$

where v_0 denotes the maximum tangential velocity at the core radius r_c. The ratio of the jet radius at the nozzle exit and the initial vortex core radius amounts to $r_{\text{jet}}/r_c = 1.3$ and the ratio of the maximum jet and tangential velocities at $x/B = 0.5$ to $u_{\text{jet}}/v_0 = 2.72$. In all cases dimensionless time, $t^* = t/t_0$, is normalized by the vortex time scale, $t_0 = 2r_c/v_0$. Here it is set zero at the beginning of the second simulation when the jet has reached an age of $t^* = 9$. The conversion of time to downstream distance is established employing the Taylor assumption with the experimental free stream velocity of $u_0/v_0 = 2.2$.

Fig. 1 depicts cross-sections of axial vorticity at $x/B = 0.5$ and $x/B = 1$. The undisturbed concentric vorticity contours represent the trailing vortex whereas the two opposite-signed regions of vorticity at $x/B = 0.5$ reflect the most unstable mode of the jet instability. These unstable structures burst subsequently and the jet reaches a fully turbulent state at $x/B = 1$. Fig. 2 shows axial and azimuthal vorticity contours in a perspective view at different instants of time. At $t^* = 90$ the fully turbulent jet is deflected and entrained by the vortex-induced velocity field and starts to wrap around the primary vortex. During that process the jet's vorticity is progressively stretched and rearranges to coherent – but now spiral-shaped – secondary vorticity structures (SVS) of opposite signs ($t^* = 110$).

Fig. 3 sketches how a passive tracer that initially extends radially between $4r_c$ and $6r_c$ is stretched in a Rankine vortex. At $32t_0$ the tracer completely encloses the vortex center and is stretched by a factor of 5π. In the long-term limit the passive tracer would be evenly distributed between $4r_c$ and $6r_c$. A similar stretch-rate of approximately one revolution in $30t_0$ takes place from $t^* = 90$ to 120 (see Fig. 2).

Fig. 2 shows, furthermore, that the counter-rotating secondary vortex rings approach each other driven by a self-induced propagation velocity. At the same time they increase

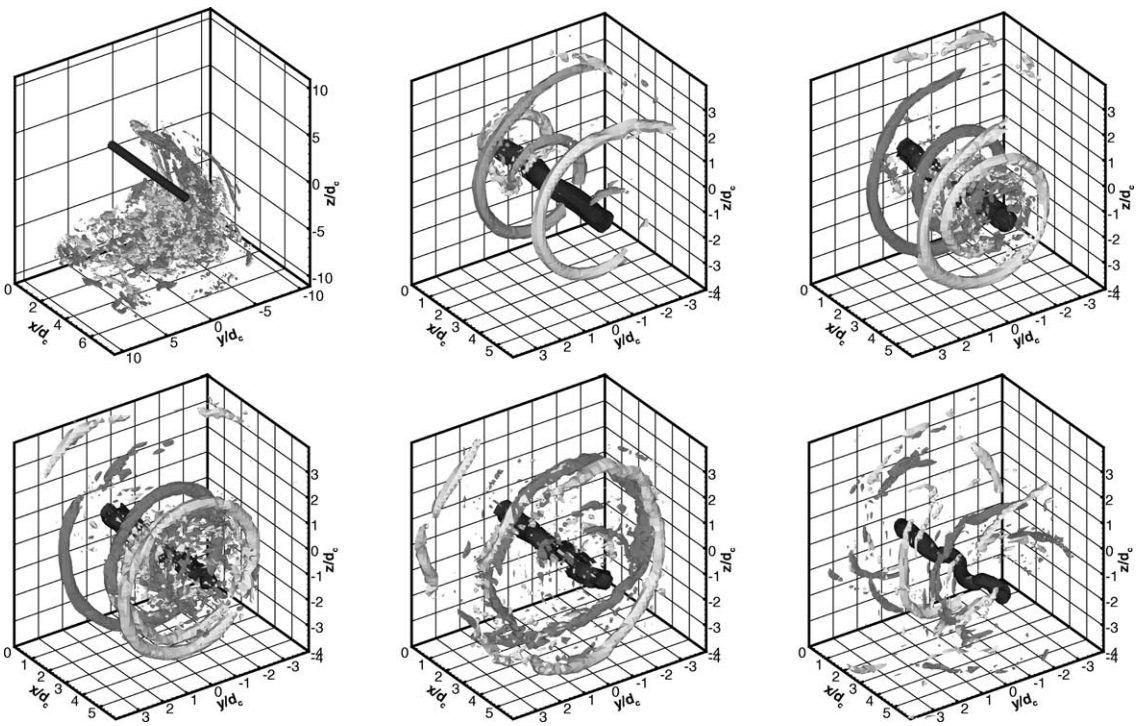

Fig. 2. Subset of the computational domain showing vorticity contours in a perspective view at $t^* = 90, 110, 120, 130, 150$, and 210 (from left to right). Black surface denotes axial component ($\omega_x^* = 3$), azimuthal components ($\omega_\theta^* = 1\ (-1)$) are plotted dark grey (light grey).

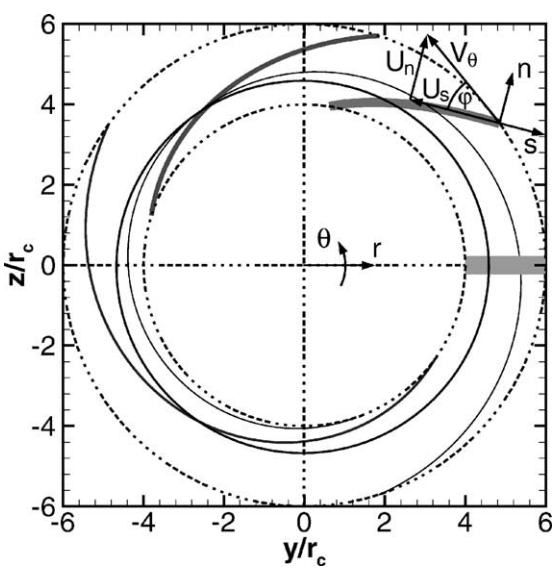

Fig. 3. Schematic of a passive tracer that initially extends between $4r_c$ and $6r_c$ and is stretched in a Rankine vortex. Different instants in time, $t = n115.2\pi^2 r_c^2/\Gamma$, are plotted at which the tracer encloses the nth part of the vortex where $n = 1/8, 1/4, 1/2$, and 1. Axisymmetric and instantaneous local Cartesian coordinate systems as well as representation of tangential velocity, V_θ, in both coordinate systems are illustrated for usage in Section 7.

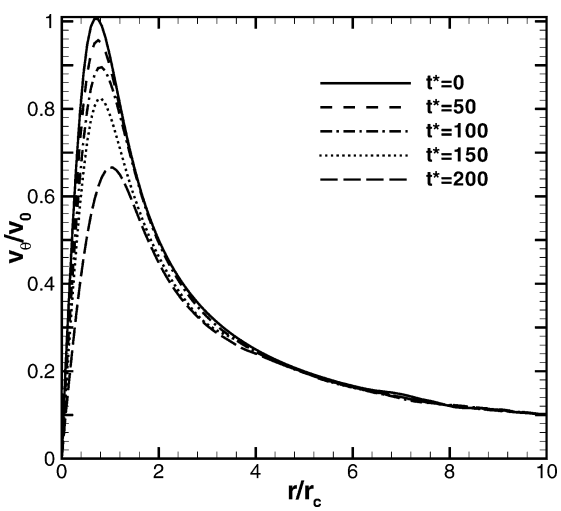

Fig. 4. Tangential velocity profiles of wake vortex at different instants in time. Velocity profiles are averaged over axial and azimuthal directions.

in radius due to mutual induction which again stretches the SVS. Finally, the counter-rotating SVS connect ($t^* = 150$) and decay by direct turbulent interaction ($t^* = 210$).

During that process the primary vortex has been stretched and deformed in turn by SVS driven induction. Fig. 4 indicates that maximum tangential velocities are progressively reduced but circulation is essentially unmodified at $r = 4r_c$ (see Fig. 5).

3. Vortex evolution in homogeneous isotropic turbulence

The effects of ambient turbulence on vortex dynamics are studied using the numerical code NTMIX3D [31] that solves the Navier–Stokes equations for a three-dimensional

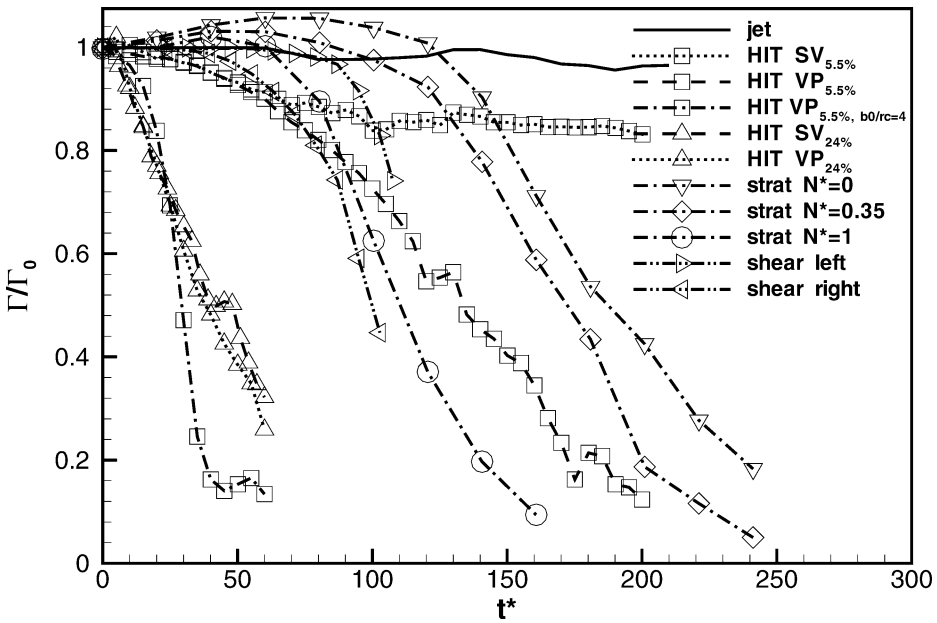

Fig. 5. Temporal evolution of axially averaged normalized circulation for all the cases. Circulations are integrated over locally centered circles with radii of $4r_c$. For vortex pair with small vortex separation ($VP_{b_0/r_c=4}$) circulation is determined on $r = b_0/2 = 2r_c$.

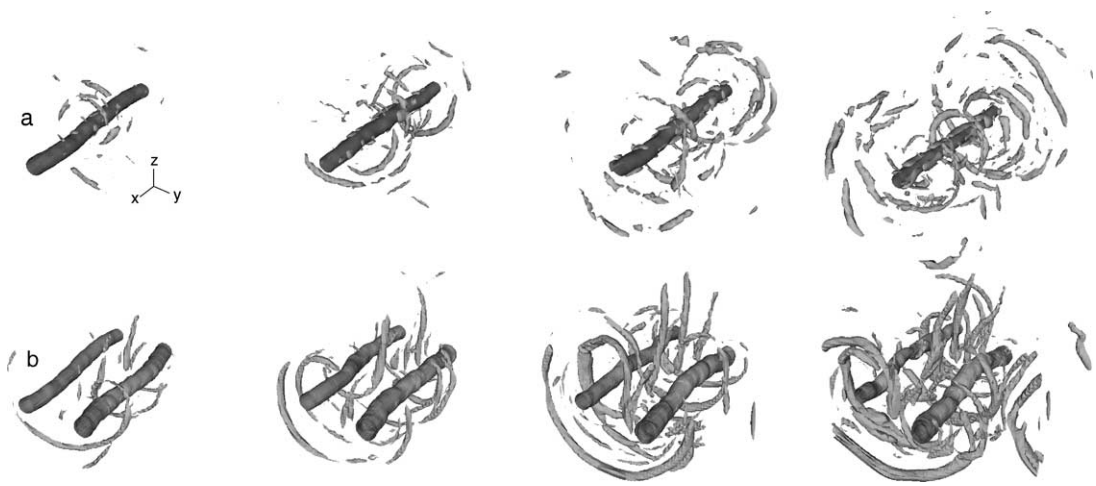

Fig. 6. Sequence of perspective views of iso-surfaces of λ_2 for vortices with $I_a = 5.5\%$ at $t^* = 25, 50, 75, 100$. (a) Single vortex, (b) vortex pair with $b_0/r_c = 8$.

unsteady flow. The code is applied in its LES version where the subgrid-scale fluxes are modeled according to the Boussinesq gradient approach and the subgrid-scale viscosity is estimated from the kinetic energy at cut-off that is assessed by the filtered structure function [4].

A field of homogeneous isotropic turbulence (HIT) is generated from a given spectrum with random phases for each mode which is subsequently allowed to adjust in a preparatory run. The resulting turbulence is characterized with respect to wake vortex parameters by the ratio of root-mean-square velocity and maximum tangential velocity of the vortex, $I_a = u'/v_0$, and the ratio of integral length scale to vortex core radius $\Lambda/r_c = 5.8$. Since the linear superposition of two Lamb–Oseen vortices may introduce additional perturbances to the flow [29], the wake vortices are allowed to form quasi-steady dipoles in a two-dimensional viscous pre-simulation. For further details regarding the numerical approach and turbulence initialization see Table 1 and [24].

Figs. 6, 9 display the temporal evolution of a single vortex (SV) and two vortex pairs (VP) with different vortex separations, b_0/r_c, for the turbulence intensity $I_a = 5.5\%$ in a sequence of perspective views of iso-surfaces of λ_2.[2] Different values for λ_2 are chosen to visualize the primary vortices and the SVS. In Fig. 6 eddies of the ambient turbulence field become visible when they are intensified

[2] The second eigenvalue λ_2 of the symmetric tensor $S^2 + \Omega^2$ is a measure for coherent vortex structures [17], where S and Ω denote the symmetric and antisymmetric parts of the velocity gradient tensor. For coherent vortex structures, the resulting λ_2 iso-surfaces largely correspond to iso-surfaces of the vorticity norm.

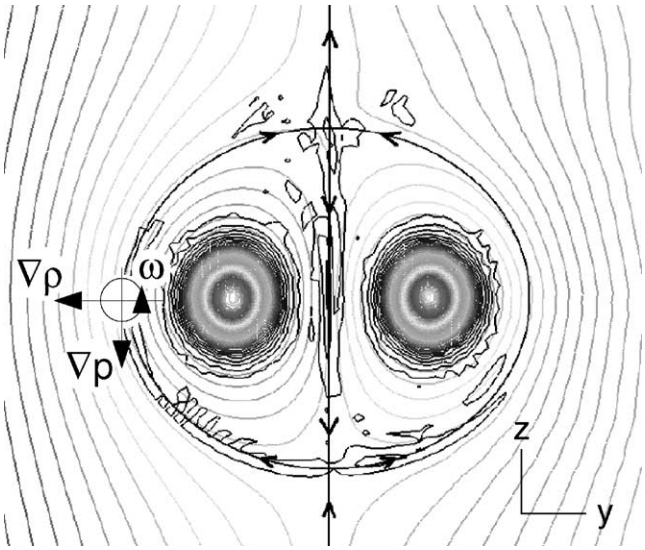

Fig. 7. Iso-lines of vorticity and streamfunction in a reference frame that descends with the vortices. Additionally, the baroclinical vorticity production in a stably stratified atmosphere is illustrated.

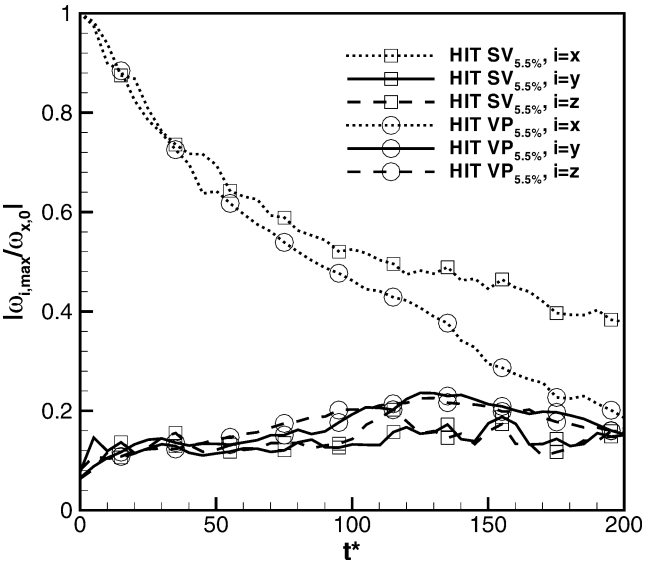

Fig. 8. Temporal evolution of the extrema of each vorticity component of the single vortex and vortex pair cases with $I_a = 5.5\%$ and $b_0/r_c = 8$. Vorticity extrema are averaged over the axial direction, x, and are normalized by the initial maximum of axial vorticity, $\omega_{x,0}$.

by vortex stretching which is induced by the primary vortices. The amount, length and intensity of the SVS increase with time. The numerous coherent SVS deform the primary vortices and lead initially to a similar decay rate in the single vortex case and the case with large vortex separation (see Fig. 5). At $t^* = 60$ the decay rates of vortex pair and single vortex start to deviate from each other and, eventually, at $t^* = 100$ the decay of the single vortex levels off. It should be noted that for the single vortex case a domain of transversally doubled size was used to assure the independence of results from the shear produced in between the single vortex and its periodic counterparts. For vortex pairs this shear is much weaker because neighbouring vortices induce velocities of the same direction and magnitude in the vicinity of the periodic boundaries.

Additionally to the mechanisms that produce SVS around a single vortex, the topology of vortex pairs provides a further mechanism that can be explained by considering streamlines in a framework that descends with the vortices (see Fig. 7). Along the streamlines that connect the two distinct hyperbolic stagnation points, the flow is accelerated and descelerated which exerts both stretching and squeezing of embedded eddies. Fig. 6 illustrates that while for the single vortex all SVS tend to be aligned azimuthally, the vortex pair produces also vertical vorticity streaks midway between the vortices (stretching by vertical gradients of the vertical velocity $\partial w/\partial z$ in the vicinity of the upper stagnation point) and oval-shaped streaks (stretching by lateral gradients of the lateral velocity $\partial v/\partial y$ in the vicinity of the lower stagnation point). These additional SVS contribute to decay by turbulent diffusion and, in particular, by exchange of vorticity in between the counter-rotating vortices. The comparison of decay rates for SV and VP in Fig. 5 indicates that the latter mechanisms advance decay effectively.

Fig. 8 depicts the evolution of the extrema of each vorticity component normalized by the initial maximum of axial vorticity, $\omega_{x,0}$ for the cases shown in Fig. 6. This representation allows to quantitatively assess the efficiency of vortex stretching mechanisms. Due to diffusion processes the axial vorticity maxima decrease with time. However, the lateral and vertical vorticity maxima, $\omega_{y,\max}$, $\omega_{z,\max}$, which at $t^* = 0$ represent eddies of the background turbulence, increase with time, driven by vortex stretching, and roughly triplicate initial values around $t^* = 125$. $\omega_{y,\max}$ and $\omega_{z,\max}$ are of similar magnitude throughout the whole evolution, because the SVS appear alternately in both components. Since the vortex pair exerts stretching both across (cf. Fig. 3) and along (cf. Fig. 7) streamlines, its vorticity maxima grow faster and maintain higher values than in the single vortex case. Finally, all vorticity components of the vortex pair have decayed to a similar level at $t^* = 200$, when circulation is reduced to 20%. The vorticity extrema of the case SV start to deviate from those of case VP at approximately $t^* = 60$, a time that correlates well to the deviation of the respective circulation evolutions (see Fig. 5). At $t^* = 100$, when the circulation of case SV remains almost constant, the decay of ω_x is reduced and the SVS are not further stretched, i.e. vorticity values $\omega_{y,\max}$, $\omega_{z,\max}$ merely fluctuate around constant values.

When vortex separation is reduced, the evolution of the circulation shows a very different decay behaviour. After a short phase of gradual decay governed by turbulent diffusion, the elliptic/short-wave instability [20,21] is developing weakly (linear phase) (see Fig. 9). Subsequently, for $t^* > 15$ the Crow/long-wave instability is largely amplified and the circulation starts to decay rapidly (which in part is due to the fact that circulation is only determined from the vorticity

Fig. 9. As Fig. 6 for vortex pair with $b_0/r_c = 4$ at $t^* = 15, 25, 50$.

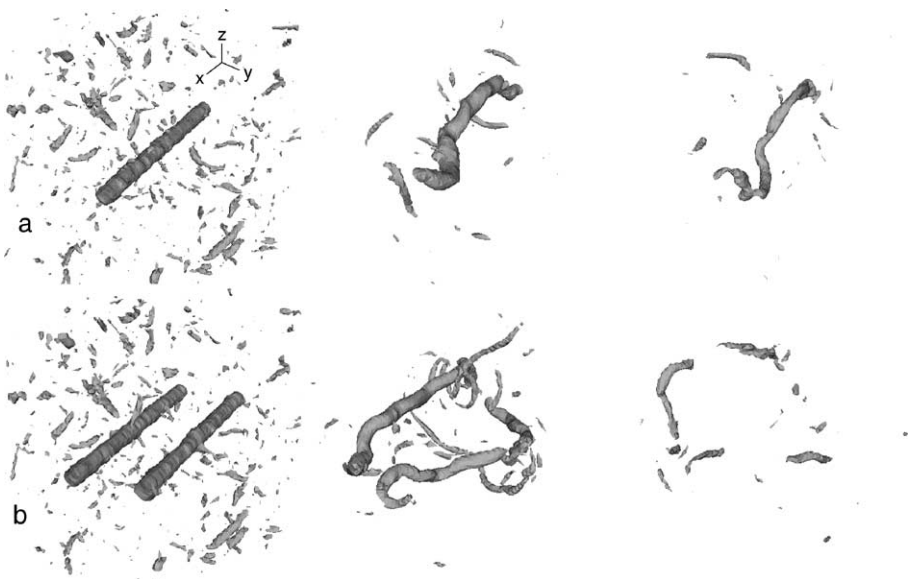

Fig. 10. Sequence of perspective views of iso-surfaces of λ_2 for (a) a single vortex and (b) a vortex pair with $I_a = 24\%$ and $b_0/r_c = 8$ at $t^* = 0, 30, 60$.

component aligned with the flight direction). After reconnection of the two primary vortices at $t^* = 25$ a vortex ring is formed at $t^* = 50$. This ring remains coherent for a certain time but deforms under its own induction and loses strength.

In the highly turbulent case ($I_a = 24\%$) depicted in Fig. 10 the primary vortices are too weak to essentially stretch the turbulent eddies. Here it is the strong ambient turbulence that directly deforms and destroys the vortices rapidly. No differences between the decay of the vortex pair and the single vortex are seen (see also Fig. 5). This indicates that interactions between the vortices of the vortex pair do not contribute to decay in strong turbulence.

4. Vortex decay in a turbulent stably stratified atmosphere

The large-eddy simulation code LESTUF which solves the Boussinesq-approximated Navier–Stokes equations and uses the classical Smagorinsky closure is employed to simulate wake vortex evolution in a thermally stably stratified atmosphere with superimposed moderate, anisotropic, and decaying turbulence. The turbulence, which is described in detail in [8], obeys prescribed spectra with $I_a = 3.6\%$, and $\Lambda/r_c = 12$. Turbulence induced by the aircraft is superimposed on the vortices by adding initially three-dimensional random perturbations with a maximum turbulence intensity of $I_v = 12\%$ at the core radius. The prescribed mean potential temperature gradient of the atmosphere, $d\Theta/dz$, is constant in each calculation and the corresponding normalized Brunt–Väisälä frequencies $N^* = (g/\Theta_0 \cdot d\Theta/dz)^{1/2}(2\pi b_0^2/\Gamma_0)$ are set to 0, 0.35, and 1. The pair of superimposed Lamb–Oseen vortices is initialized with a ratio of $b_0/r_c = 12$ for which a self-adaption phase is not necessary because the resulting distortions are weak [29]. For further details regarding the numerical set-up we refer to [14] and Table 1.

Fig. 11 depicts iso-contours of the lateral and vertical vorticity components that are induced by the wake vortices (represented by tubular λ_2-contours) in a stably stratified turbulent atmosphere for two degrees of stratification. In the case $N^* = 0.35$, the iso-lines of the lateral velocity, v, illustrate the converging flow that is induced by the wake vortices. This converging flow is deformed by turbulence such that the iso-line $v = 0$ (bold) meanders along the symmetry plane between the vortices. As described in quantitative detail in [14], such a superposition of turbulent and wake vortex induced velocities produces axial gradients of the lateral velocity, $\partial v/\partial x$, and, equivalently, vertical vorticity, $\omega_z \sim \partial v/\partial x$ in a volume above and midway

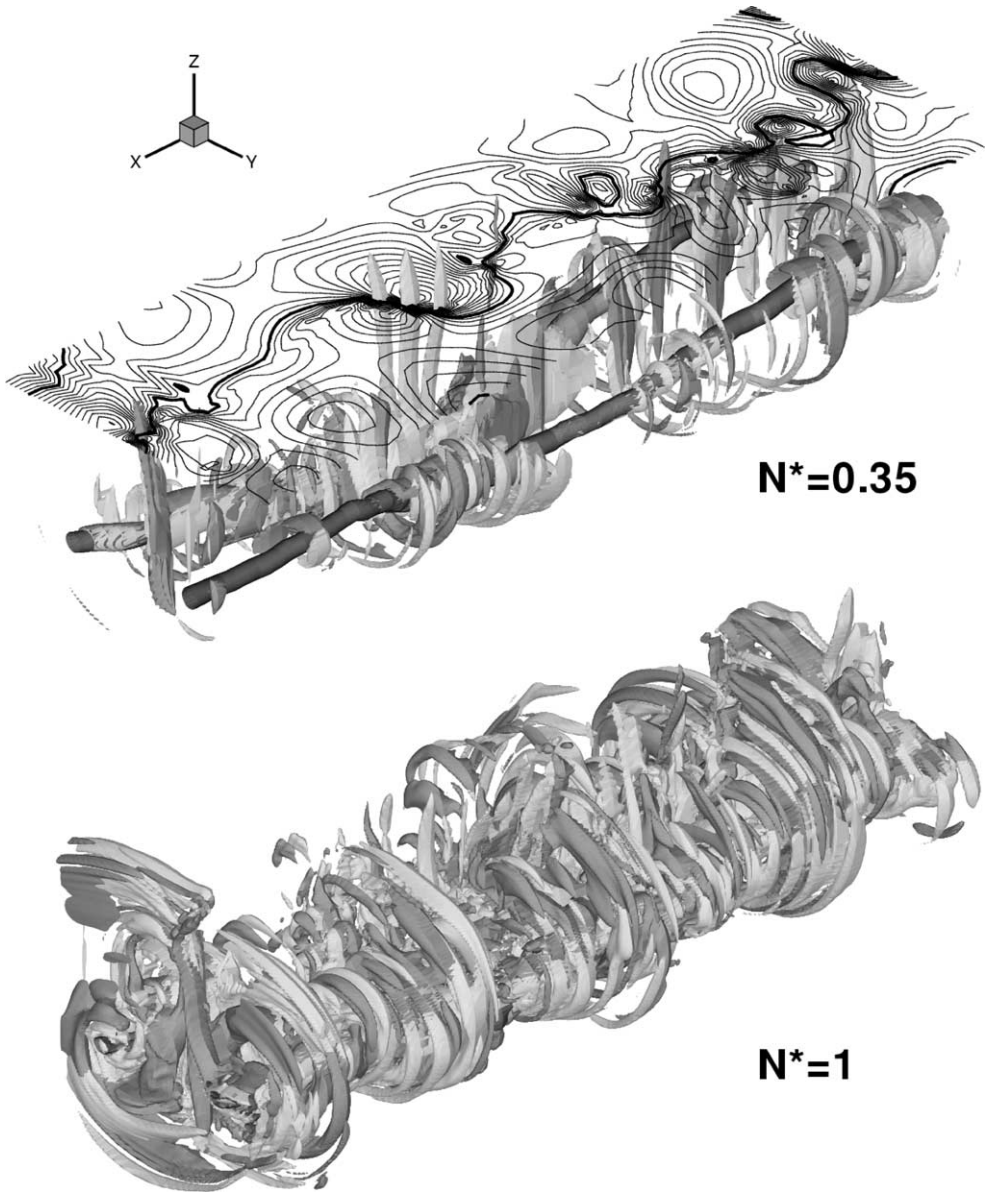

Fig. 11. Wake vortex evolutions in a turbulent and weakly stratified ($N^* = 0.35$) and in a turbulent and strongly stratified ($N^* = 1$) atmosphere at $t^* = 120$. Iso-surfaces of lateral and vertical vorticity components ($\omega_y^* = \omega_z^* = 0.125$ (-0.125) plotted dark grey (light grey)) in a perspective view. Wake vortices are represented by black tubular λ_2-contours. For $N^* = 0.35$, iso-lines for lateral velocity, v, are plotted in a horizontal plane above the vortices.

between the vortices. The resulting vertical vorticity streaks, ω_z, are amplified by vortex stretching due to the acceleration of the downwards directed flow between the main vortices. Then, the vorticity is tilted, and wraps around the primary vortices.

The intense SVS in Fig. 11 below demonstrate that strong stable stratification ($N^* = 1$) intensifies these effects considerably. The source of this intensification is the baroclinical vorticity, ω_x, which is produced by the baroclinic torque according to

$$\frac{D\omega_x}{Dt} \sim \frac{1}{\rho^2}\nabla\rho \times \nabla p \tag{2}$$

along the oval-shaped interface (see Fig. 7) between the ambient flow and the adiabatically heated flow that descends with the vortices [13]. This baroclinical vorticity additionally induces lateral velocities above the vortices that are directed towards the symmetry plane. Herewith it intensifies the axial gradients of the lateral velocity which finally cause the vertical and azimuthal vorticity structures and the related decay. Fig. 5 quantifies the impact of a stably stratified atmosphere on the longevity of wake vortices.

5. Wake vortices in a turbulent environment with constant shear

Shear flows exhibit vigorous and variform influences on wake vortex transport and decay. Wake vortices that interact

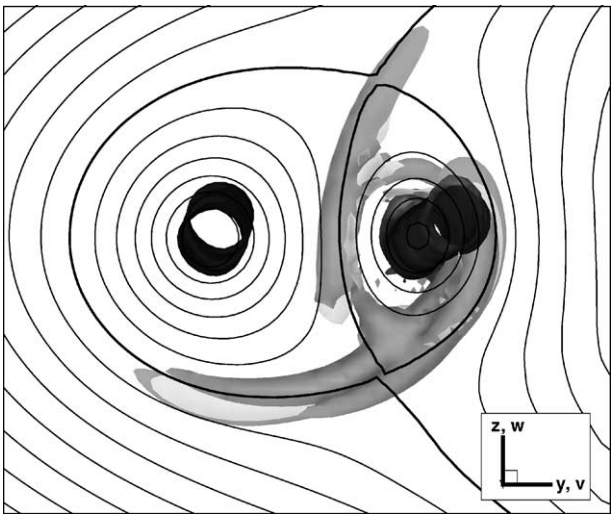

Fig. 12. Axial view of wake vortices in a turbulent environment with constant positive background shear at $t^* = 47$. Iso-surfaces of lateral and vertical vorticity components ($\omega_y^* = \omega_z^* = 0.63$ (-0.63) plotted dark grey (light grey)); wake vortices represented by black tubular λ_2-contours. Streamlines in a reference system that moves with the vortices in the plane $x = L_x/2$.

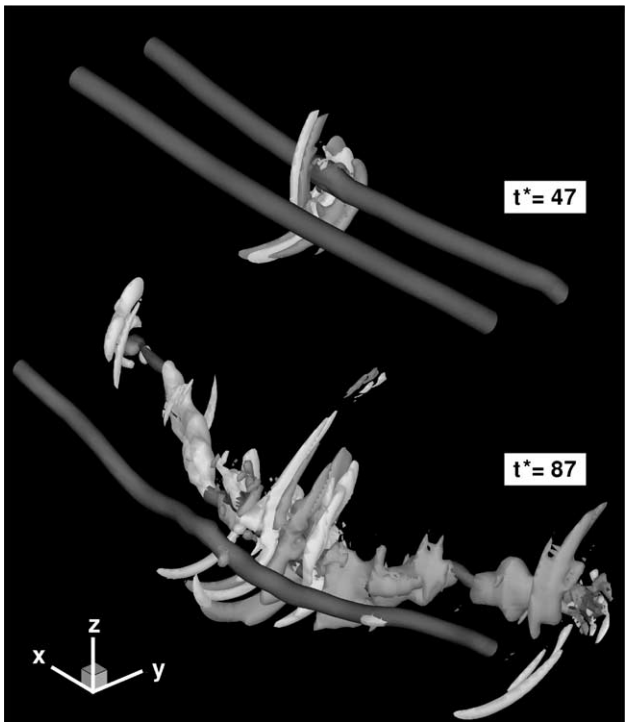

Fig. 13. Wake vortices in turbulent sheared environment in a perspective view. Iso-surfaces as in Fig. 12.

with a shear layer may experience vortex tilting, separation and subsequent rebound of vortices, whereupon the vortex with opposite signed vorticity to the shear layer shows the stronger tendency to rebound [25]. It is again the vortex with opposite-signed vorticity that decays distinctly faster when the vortex pair immerges into a turbulent shear-layer [12]. Also the spectacular rebound observed at London-Heathrow Int'l Airport [10] can be at least in part attributed to shear-layer effects [15]. However, these effects are not observed in laminar flows with constant shear [11].

Here, we report a DNS of vortex evolution in a constantly sheared and turbulent environment. For this purpose the code MESOSCOP [28] is employed which solves the Boussinesq-approximated Navier–Stokes equations. The pair of Lamb–Oseen vortices with a vortex spacing of $b_0/r_c = 8$ is perturbed sinusoidally with an amplitude of $0.01b_0$ at the wavelength of $8.6b_0$ to trigger the Crow instability which allows to study the influence of vortex spacing on decay. The weak homogenous and initially isotropic ambient turbulence is characterized by $I_a = 0.7\%$, and $\Lambda/r_c \approx 8$. The prescribed constant background strain just compensates the strain that the left vortex would induce on the right vortex center. Employing the common normalization for vortex pairs the shear corresponds to $(\partial v/\partial z)(2\pi b_0^2/\Gamma_0) = 1$.

Fig. 12 shows the wake vortices represented by black tubular λ_2-contours in an axial view. The corresponding streamlines indicate an intrinsic asymmetry of the vortex flow, as known from analytical investigations of wake vortices subjected to background shear [3] (compare Fig. 7 for the unsheared case). The formation of SVS (grey iso-surfaces of lateral and vertical vorticity) is in striking correlation with the streamline that separates the fluid in and outside the vortex oval. The right vortex, which is composed of opposite signed vorticity compared to the background vorticity of the shear, is closely encompassed by the SVS. A vertical streak evolves above the vortex pair that lags progressively behind the descending vortices because it develops partially outside the oval that descends with the vortices. This structure is similar as in unsheared cases (cf. Fig. 11) but here it is deflected to the right due to the advection by the background shear flow.

The perspective view for two different instants, depicted in Fig. 13, gives a spatial impression of the evolution of the flow structures. At $t^* = 47$ the SVS indicate that vortex stretching of ambient turbulence is most effective near the right vortex at the axial position where the vortices are closest. At this particular position the area around the right vortex which is enclosed by the bold separating streamline achieves the smallest size (cf. Fig. 12). Consequently, the SVS structures that extend from the stagnation points (i) have to cover a small distance to completely encompass the vortex and (ii) the SVS experience strong acceleration and, hence, strong stretching in the vicinity of the right vortex. Fluid, almost at rest at the stagnation point, follows the streamlines to locations of high circumferential velocity in close proximity to the right vortex core, resulting in strong acceleration. Contrary to non-sheared cases, the distance between left vortex (same signed vorticity as the background shear) and vortex oval boundary is increased, which gives an explanation for unbalanced decay rates and prolongated lifetimes of the vortices [11].

At $t^* = 87$ SVS have formed all along the right vortex and have initiated a rapid decay phase (see Fig. 5). As a

result of the initial perturbation the vortices link at about $t^* = 100$ which initiates rapid decay also for the left vortex. This is combined with tilting of the closely spaced vortex segments caused by mutual induction of the unequally strong vortices.

6. Comparison of decay characteristics

So far we employed normalized time based on the vortex time scale, $t_0 = 2r_c/v_0$, to allow for the comparison of decay characteristics of both single vortex and vortex pair cases (see Fig. 5). We found in Section 3 that a reduction of normalized vortex spacing by a factor of two may accelerate decay by a factor of four. Alternatively, we now employ the normalization of time that is commonly used for vortex pairs and is based on the time scale $t_0 = 2\pi b_0^2/\Gamma_0$. Fig. 14 indicates that now the decay rates of the two cases HIT, $I_a = 5.5\%$ with a variation of vortex separation by a factor of two almost coincide. This means that the time normalization for vortex pairs considers the effects of vortex separation correctly even when the underlying decay mechanisms may differ considerably (cf. Figs. 6, 9). Another consequence is that increasing vortex core radii for a given vortex separation reduces lifetime only slightly, whereas a reduction of b_0 may be very beneficial for an accelerated vortex decay.

A comparison of all cases in Fig. 14 indicates that the life span of the vortices is basically correlated to the intensity of ambient turbulence. However, the specific pecularities of the different cases, like additional superposition of aircraft-induced turbulence in the stratified cases or initial perturbation of the vortex spacing in the sheared case, modify the ranking according to background turbulence. Imposing additionally a stable temperature stratification with $N^* = 1$ may reduce wake vortex lifetime by roughly two time units whereas an increase of ambient turbulence from $I_a = 5.5\%$ by a factor of four may shorten wake vortex life by four time units. In contrast, dimensional analysis tells us that the life span of wake vortices in a given environment may be halved by a reduction of vortex spacing by a factor of $\sqrt{2}$.

7. Formation of secondary vorticity and decay mechanisms

As shown in the previous sections the formation of coherent secondary vorticity around the primary vortices is a prominent feature of wake vortex evolution in the atmosphere. In the following we list common aspects of the related mechanisms.

(i) Incoherent vorticity of background turbulence achieves coherence by tilting and stretching. It is the primary vortex that alignes (tilting) and reinforces (stretching) random vorticity such that SVS are produced.

(ii) However, a single vortex filament that is stretched will conserve its circulation (Helmholtz theorem). Hence, the vorticity of the vortex filament may be increased considerably by stretching, but its far field effect in terms of velocity induction is not modified.

(iii) Although the merger of several coherent vorticity filaments of equal sign may generate larger SVS, this mechanism likewise does not amplify far field effects.

(iv) Far field velocity induction (circulation) is generated and increased when vorticity of arbitrary orientation which has no far field effect is aligned to coherent structures by the tilting process.

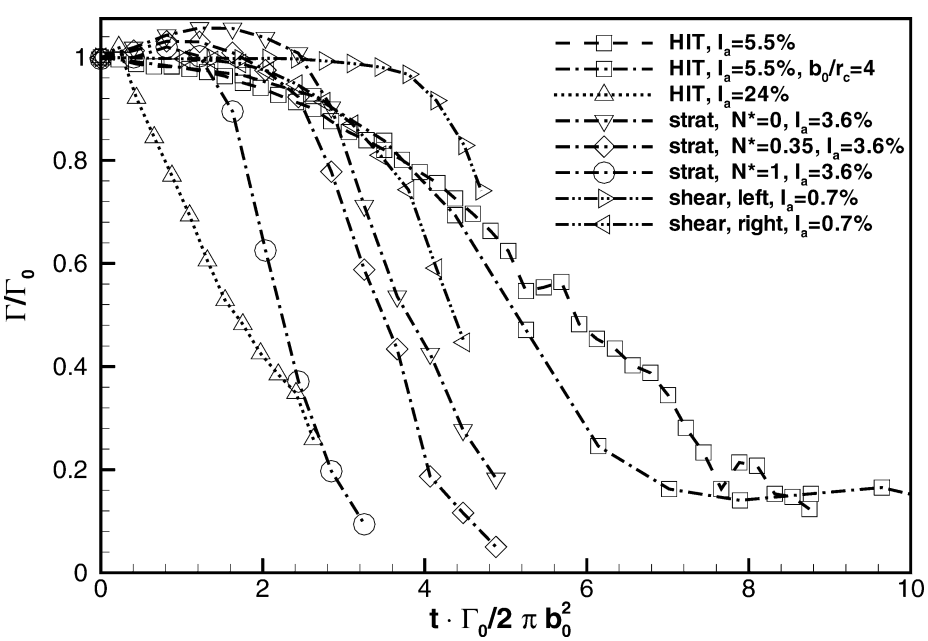

Fig. 14. Temporal evolution of normalized circulation where the common normalization of time for vortex pairs is employed. Circulations determined as in Fig. 5.

(v) The tilting mechanism is effective for any vorticity structure that at least contains some radial vorticity component and (vi) tilting provokes simultaneous stretching. This can be illustrated by considering vortex tilting and stretching in a background flow given by a single plane potential vortex, $V_\theta(r) = \Gamma/(2\pi r)$. Viscous and baroclinic effects are neglected.

For convenience, the secondary vorticity, ω_s, is given in an instantaneous local Cartesian coordinate system with direction s along the spiral-shaped vortex line, and n away from the center of curvature (cf. Fig. 3). The tilting and stretching terms read

$$\frac{D\omega_n}{Dt} = \omega_s \frac{\partial U_n}{\partial s}, \qquad \frac{D\omega_s}{Dt} = \omega_s \frac{\partial U_s}{\partial s}, \tag{3}$$

where the velocity gradients along the vortex line, $\partial U_n/\partial s$, $\partial U_s/\partial s$, are prescribed by the background flow $V_\theta(r)$. For the tilting term it follows

$$\begin{aligned}\frac{D\omega_n}{Dt} &= \omega_s \frac{\partial U_n}{\partial r}\frac{\partial r}{\partial s} = \omega_s \frac{\partial (V_\theta \sin\varphi)}{\partial r}\frac{\partial r}{\partial s} \\ &= \omega_s \frac{\Gamma}{2\pi r^2}\sin^2\varphi,\end{aligned} \tag{4}$$

where φ denotes the angle between V_θ and U_s. In analogy the stretching term yields

$$\begin{aligned}\frac{D\omega_s}{Dt} &= \omega_s \frac{\partial U_s}{\partial r}\frac{\partial r}{\partial s} = \omega_s \frac{\partial (V_\theta \cos\varphi)}{\partial r}\frac{\partial r}{\partial s} \\ &= \omega_s \cos\varphi \frac{\Gamma}{2\pi r^2}\sin\varphi.\end{aligned} \tag{5}$$

Eqs. (4) and (5) specify the limits of the processes: Tilting is strongest for radially oriented vorticity filaments because $\partial r/\partial s = \sin\varphi = 1$ and tilting ceases for azimuthally oriented structures because in azimuthal direction $\sin\varphi = 0$. Radially aligned filaments are not yet stretched because $\cos\varphi = 0$, whereas azimuthally oriented structures can not be further stretched ($\sin\varphi = 0$). In summary, radially oriented vorticity is first tilted and then tilted and stretched simultaneously until both processes decay when in the long-term limit the SVS tend to be aligned azimuthally.

(vii) SVS can deform primary vortices. In particular, counter-rotating SVS can stretch (squeeze) the primary vortices when approaching (departing from) each other (see Fig. 2, $t^* = 210$).

(viii) In a reference frame that descends with the vortex pair the vortices are engulved by a oval-shaped streamline with stagnation points below and above the vortices (see Fig. 7). Due to the low velocities at the stagnation points already minor disturbances are sufficient to displace the stagnation points which enables entrainment of ambient vorticity into the oval (see Fig. 11). Entrained vorticity is subsequently intensified according to the right equation in (3) by vortex stretching along streamlines in the accelerated flow midway between the vortices or along the half moon shaped streamlines around the vortices.

(ix) Counter-rotating vorticity streaks produced midway between the vortices can be effective in exchanging fluid across the symmetry line. This effect is prerequisite for direct cancelation of primary vorticity [3,14].

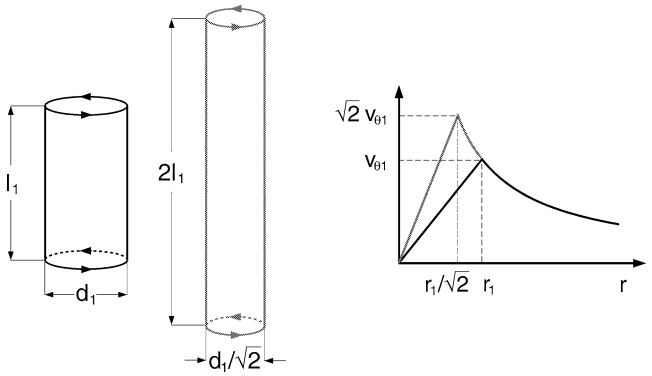

Fig. 15. Sketch to illustrate the increase of rotational energy of a stretched Rankine vortex.

(x) A primary vortex that stretches SVS as depicted in Fig. 3 performes work on the SVS. During the stretching process the SVS gain rotational energy, whereas the primary vortex, in turn, loses rotational energy. This can be delineated phenomenologically by considering a vortex tube with a Rankine tangential velocity distribution that is stretched by a factor of 2 (see Fig. 15). The increase in length corresponds to a contraction by a factor of $1/\sqrt{2}$ (mass conservation). During stretching angular momentum is conserved ($r v_\theta = \text{const.}$), which means that the potential vortex region is not affected by stretching. But the angular velocity of the contracted vortex core is doubled according to $\Omega_2 = r_1^2/r_2^2 \Omega_1$ because $r_2 = r_1/\sqrt{2}$. The work performed on the vortex core, $W_{1,2}$, which corresponds to its gain of rotational energy, ΔE, amounts to

$$\begin{aligned}W_{1,2} &= E_2 - E_1 = \frac{1}{2}\left(m\frac{r_2^2}{2}\Omega_2^2 - m\frac{r_1^2}{2}\Omega_1^2\right) \\ &= \frac{1}{2}\left(m\frac{r_1^2}{4}4\Omega_1^2 - m\frac{r_1^2}{2}\Omega_1^2\right) = E_1.\end{aligned} \tag{6}$$

Hence, a doubling of length corresponds directly to a doubling of rotational energy of the flow in the vortex core of the SVS. The described mechanism is in direct analogy to the energy transfer from large eddies to small eddies in turbulent flows [32]. In our cases it is most obvious in the jet vortex interaction where rotational energy of the primary vortex decreases only on smaller radii (Fig. 4) and in the low-turbulence cases of Section 3 (Figs. 5, 6, 8). In particular, in the single vortex case HIT $SV_{5.5\%}$ circulation decay ends at a time of $t^* = 100$ when the SVS are not further stretched.

(xi) The formation of SVS may trigger the formation of cooperative instabilities as the short-wave instability [21] and the Crow [2] instability.

With the exception of cooperative instabilities the described mechanisms are independent from the ratio of vortex core radius and vortex separation. We therefore assume that the relatively large vortex cores that we used here and that are commonly employed in numerical simulations do not derogate the current results.

8. Conclusions

The presented numerical simulations of wake vortex evolution in the atmosphere indicate that stretching, tilting and merger of ambient vorticity caused by the primary vortices are the prominent mechanisms in vortex evolution and decay. In the cases with low to moderate turbulence possibly combined with thermal stable stratification and/or constant shear as well as with jet–vortex interactions these mechanisms create spatially and temporarily extended coherent secondary vortices out of the ambient incoherent flow. At first, the creation of these secondary vorticity structures consumes energy of the primary vortices. Secondly, the secondary vorticity structures, in turn, have a far field impact, and thus, deform the primary wake vortices. It is shown that these mechanisms lead to an initially gradual and subsequent rapid decay. Whereas continous decay can be attributed to diffusion and the work that the primary vortices perform on the secondary vorticity structures, rapid decay is associated with the interaction of secondary vorticity with the primary vortex pair which causes an exchange and mutual annihilation of primary vorticity, also in combination with instability mechanisms and the transition to fully turbulent vortices. For single vortices, longitudinal stretching of secondary vorticity and the mutual exchange of primary vorticity between counter-rotating vortex pairs does not apply. Therefore, the decay of single vortices is strongly reduced when the energy transfer from primary to secondary vortices ceases because the secondary vortices are no longer stretched substantially when they tend to be aligned azimuthally. In a highly turbulent atmosphere, the primary vortices are too weak and the time scales of vortex decay are too short to essentially stretch atmospheric eddies. As a consequence, the wake vortices are rapidly disrupted directly by ambient turbulence.

It should be noted that numerical simulations of wake vortices in the atmosphere unavoidably suffer from limited resolution of the vortex core region. Whereas DNS only reach small Reynolds numbers it is the type of subgrid-scale closure that controls vortex core evolution in LES [15]. Both approaches do not meet the complex interaction of turbulence and rotation at high *Re* flows together with the peculiarities of specific aircraft configurations and environmental conditions. This limitation will persist despite the enormous increase of computational power and the development of smart numerical methods. Full-scale experiments will remain both challenging and mandatory to ensure the validity of the conclusions drawn from numerical simulations.

References

[1] S. Brunet, L. Jacquin, P. Geffroy, Experiment on heated jets/wake vortex interaction, ONERA RT 15/2496 DAFE/Y, 1999.
[2] S.C. Crow, Stability theory for a pair of trailing vortices, AIAA J. 8 (1970) 2172–2179.
[3] C.P. Donaldson, A.J. Bilanin, Vortex wakes of conventional aircraft, AGARDograph 204, 1975.
[4] F. Ducros, P. Comte, M. Lesieur, Large-eddy simulation of spatially growing boundary layer over an adiabatic flat plate, Internat. J. Heat Fluid Flow 16 (1995) 341–348.
[5] F. Garnier, F.C. Beaudoin, P. Woods, N. Louisnard, Engine emission alteration in the near field of an aircraft, Atmosph. Environ. 31 (1997) 1767–1781.
[6] C. Ferreira Gago, S. Brunet, F. Garnier, Numerical investigation of turbulent mixing in a jet/wake vortex interaction, AIAA J. 40 (2002) 276–284.
[7] T. Gerz, T. Ehret, Wingtip vortices and exhaust jets during the jet regime of aircraft wakes, Aerosp. Sci. Technol. 1 (1997) 463–474.
[8] T. Gerz, F. Holzäpfel, Wingtip vortices, turbulence, and the distribution of emissions, AIAA J. 37 (1999) 1270–1276.
[9] T. Gerz, F. Holzäpfel, D. Darracq, Commercial aircraft wake vortices, Prog. Aerosp. Sci. 38 (2002) 181–208.
[10] J.S. Greenwood, J.M. Vaughan, Measurements of aircraft wake vortices at Heathrow by laser doppler velocimetry, Air Traffic Control Quarterly 6 (1997) 179–203.
[11] T. Hofbauer, Numerische Untersuchungen zum Einfluss von Windscherung und Turbulenz auf Flugzeugwirbelschleppen, Ph.D. Dissertation, DLR, Oberpfaffenhofen, 2002.
[12] T. Hofbauer, T. Gerz, Shear-layer effects on the dynamics of a counter-rotating vortex pair, AIAA Paper 2000-0758, 2000.
[13] F. Holzäpfel, T. Gerz, Two-dimensional wake vortex physics in the stably stratified atmosphere, Aerosp. Sci. Technol. 3 (1999) 261–270.
[14] F. Holzäpfel, T. Gerz, R. Baumann, The turbulent decay of trailing vortex pairs in stably stratified environments, Aerosp. Sci. Technol. 5 (2001) 95–108.
[15] F. Holzäpfel, T. Hofbauer, T. Gerz, U. Schumann, Aircraft wake vortex evolution and decay in idealized and real environments: methodologies, benefits and limitations, in: R. Friedrich, W. Rodi (Eds.), Advances in LES of Complex Flows, Kluwer, Dordrecht, 2002, 2002, pp. 293–309.
[16] F. Holzäpfel, T. Gerz, F. Köpp E. Stumpf, M. Harris, R.I. Young, A. Dolfi-Bouteyre, Strategies for circulation evaluation of aircraft wake vortices measured by lidar, J. Atmos. Ocean. Tech., accepted for publication.
[17] F. Jeong, J. Hussain, On the identification of a vortex, J. Fluid Mech. 285 (1995) 69–94.
[18] H.-J. Kaltenbach, T. Gerz, U. Schumann, Large-eddy simulation of homogeneous turbulence and diffusion in stably stratified shear flow, J. Fluid Mech. 280 (1994) 1–40.
[19] L. Kleiser, U. Schumann, Spectral simulations of the laminar-turbulent transition process in plane poiseuille flow, in: Spectral Methods for Partial Differential Equations, SIAM, Philadelphia, 1984, pp. 141–163.
[20] F. Laporte, D. Darracq, A. Corjon, On the vortex-turbulence interaction: DNS of elliptic instability of a vortex pair, AIAA Paper 99-3417, 1999.
[21] T. Leweke, C.H.K. Williamson, Cooperative elliptice instability of a vortex pair, J. Fluid Mech. 360 (1998) 85–119.
[22] R.C. Miake-Lye, M. Martinez-Sanchez, R.C. Brown, C.E. Kolb, Plume and wake dynamics, mixing and chemistry behind a high speed civil transport, J. Aircraft 30 (1993) 467–479.
[23] A. Michalke, G. Hermann, On the inviscid instability of a circular jet with external flow, J. Fluid Mech. 114 (1982) 343–359.
[24] H. Moet, D. Darracq, F. Laporte, A. Corjon, Investigation of ambient turbulence effects on vortex evolution using LES, AIAA Paper 2000-0756, 2000.
[25] F.H. Proctor, D.A. Hinton, J. Han, D.G. Schowalter, Y.-L. Lin, Two-dimensional wake vortex simulations in the atmosphere: Preliminary sensitivity studies, AIAA Paper 97-0056, 1997.
[26] F.H. Proctor, G.F. Switzer, Numerical simulation of aircraft trailing vortices, in: 9th Conf. on Aviation, Range and Aerospace Meteorology 7.12, 2000, pp. 511–516.
[27] F. Risso, A. Corjon, A. Stoessel, Direct numerical simulations of wake vortices in intense homogeneous turbulence, AIAA J. 35 (1997) 1030–1040.

[28] U. Schumann, T. Hauf, H. Höller, H. Schmidt, H. Volkert, A mesoscale model for the simulation of turbulence, clouds and flow over mountains: Formulation and validation examples, Beitr. Phys. Atmosph. 60 (1987) 413–446.

[29] D. Sipp, L. Jacquin, C. Cossu, Self-adaption and viscous selection in concentrated two-dimensional vortex dipoles, Phys. Fluids 12 (2000) 245–248.

[30] P.R. Spalart, Airplane trailing vortices, Annu. Rev. Fluid Mech. 30 (1998) 107–138.

[31] A. Stoessel, An efficient tool for the study of 3d turbulent combustion phenomena on MPP computers, in: Proceedings of the HPCN 95 Conference, Springer-Verlag, 1995, pp. 306–311.

[32] H. Tennekes, J.L. Lumley, A First Course in Turbulence, MIT Press, Cambridge, MA, 1972.